

Elongation Effect on Beta-induced Alfvén Eigenmodes

Gengxian Li¹, Yueyan Li², Yong Xiao^(1*)

¹ Institute for Fusion Theory and Simulation, Zhejiang University, Hangzhou, 310027, China

² National Supercomputing Center in Tianjin, China

*(Corresponding author) Email: yxiao@zju.edu.cn

Abstract:

Beta induced Alfvén eigenmode (BAE) can be an important candidate for ion loss in burning plasmas. Elongation effect on BAE has been investigated by the gyrokinetic eigenvalue code DAEPS in this work. We construct a shaped equilibrium model by modifying local $s - \alpha$ model with which the capability of the DAEPS code has been extended to study the elongation effect. It is discovered that the BAE growth rate first increases with elongation factor κ , reaches a maximum and then decreases. This trend occurs for many different values of η_i . We find that, in the weak or moderate elongation region, the BAE instability is reactive type and mainly determined by the fluid/MHD effects, namely the combination of stabilizing field line bending term and destabilizing interchange drive in the vorticity equation. However, in the strong elongation region, the BAE instability becomes dissipative and is mainly driven by the wave-particle resonance effect embeded in δW_k since the fluid driving damps away. It is also discovered that the wave-particle resonance decreases with elongation in this region, which is due to the decrease of the geodesic curvature with elongation and leads to the decrease in the growth rate of BAE.

I . INTRODUCTION

Energetic particles (EPs) can destabilize various Alfvén eigenmodes (AEs), which in turn can substantially degrade the confinement for the energetic particles. The common Alfvén eigenmodes include toroidicity induced Alfvén Eigenmode (TAE)[1–3], beta induced Alfvén Eigenmode (BAE)[4–6], energetic particle mode (EPM)[7], reversed shear Alfvén eigenmode (RSAE)[8,9], etc. Among them, BAE has a low characteristic frequency in the beta-induced gap in the shear Alfvén continuous spectrum, which is caused by the coupling between the toroidal Alfvén wave and ion sound wave. BAE could lead to a major ion loss in fusion device, and it can be destabilized by either energetic particles or thermal ions. The BAE mode has been observed by DIII-D tokamak experiments, where an Alfvénic instability with the BAE frequency is excited by neutral beam injection only in high beta plasmas[10]. Progress has been made in theory and simulation of the BAE mode during the last two decades[6,11]. For example, with the asymptotic matching method, an analytic theory has been developed to investigate the BAE linear instability based the $s - \alpha$ model with concircular magnetic fluxes[12]. Recently both fluid-kinetic hybrid simulation and gyrokinetic simulation have been

43 developed to look into the linear and nonlinear BAE physics[4,13–15]. Here we
44 employ a newly developed non-perturbative linear eigenvalue code named
45 DAEPS[16] (drift Alfvén energetic particle stability) to investigate the plasma
46 shaping effect on the BAE instability.

47 The DAEPS code is based on the general fishbone-like dispersion relation
48 (GFLDR) theoretical framework and uses the numerical method of finite element
49 to calculate various unstable or stable drift Alfvénic eigenmodes in toroidal
50 plasmas[16]. This code uses an iteration method to solve the vorticity equation, as
51 well as to obtain the complex frequency ω and asymptotic behaviour Λ with
52 high precision. In addition, it has used the Neumann boundary condition for
53 accurate asymptotic wave behaviour in the inertial region of the ballooning space,
54 i.e., $\partial_\theta \Psi = i\Lambda\Psi$. Many numerical codes have investigated the AE physics by setting
55 the perturbed magnetic potential $\Psi = 0$ as the boundary condition[17,18],
56 which cannot accurately compute the asymptotic mode behaviour and then the
57 eigen frequency on many occasions, especially for those damped modes or
58 marginally unstable modes.

59 Most previous studies on the AEs are based on a model equilibrium with
60 concircular magnetic flux surface[16,19]. However, the cross section of magnetic
61 flux surface is generally not circular in modern tokamaks. The plasma shaping
62 factors could be crucial for determining linear instability and nonlinear
63 transport[20]. Therefore, it is important to take plasma shaping factors such as
64 elongation and triangularity into account, which could be a difficult task for the
65 conventional theory. For the model equilibrium, Miller and et al have used nine
66 parameters to establish an analytic equilibrium for the D-shaped plasma[21]. Here
67 we develop a shaped equilibrium model by following Miller’s approach but only
68 focus on the elongation factor. In this equilibrium, an analytical constrain has been
69 found for important physical quantities such as Shafranov shift Δ , elongation
70 factor κ and normalized pressure gradient α . Then we implement this model in
71 the DAEPS code to investigate the elongation effect on the BAE instability. It is
72 discovered that the linear growth rate of BAE first increases and then decreases
73 with elongation factor κ . And then how the MHD and kinetic effects together affect
74 the instability of BAE has also been analyzed and discussed in detail.

75 This paper is organized as follows. In Sec. II, we show the governing equations
76 in the ballooning representation for the most general magnetic equilibrium. Then
77 we introduce a new equilibrium model with elongation factor κ and demonstrate
78 how the governing equations for drift Alfvénic instabilities are modified by the
79 elongation, where it is crucial to calculate the specific forms for the factors of κ
80 and g in governing equations and implement them in the DAEPS code. Next, Sec.
81 III presents numerical results by the DAEPS code, where we exhibit the
82 relationship between the elongation and the growth rate of BAE in various
83 situations. In Sec. IV, we analyze how the elongation affects the BAE instability
84 and make physics interpretations for the numerical results. In Sec. V, we give a
85 summary of the elongation effect on BAE mode and discuss the future work.

87 II. Theoretical model and equations

88 A. Vorticity equation and gyrokinetic equation

89 It has been known that the high- n drift-Alfvénic modes are most relevant for
90 electromagnetic turbulence in large size fusion devices such as ITER. Ballooning
91 representation is conveniently employed here to reduce the complexity of
92 calculating these high- n modes. In order to accurately address the complex
93 magnetic geometry in a tokamak, a particular set of magnetic coordinates, i.e., the
94 Boozer coordinates $(\psi_p, \theta_B, \zeta_B)$ are used in the theoretical modelling and numeric
95 calculation in this paper. The vorticity equation using the ballooning
96 representation and the Boozer coordinates can be written as[16,22]

$$\begin{aligned} \partial_\theta \kappa_\perp^2 \partial_\theta \delta\psi + \frac{1}{P_\parallel^2} \frac{\omega(\omega - \omega_{*pi})}{\omega_A^2} \kappa_\perp^2 \delta\psi + \frac{1}{P_\parallel^2} \alpha g \delta\psi \\ = \sum_j \left\langle \frac{4\pi q_j q^2 R^2}{k_\theta^2 c^2 P_\parallel^2} J_0(k_\perp \rho_j) \omega \omega_{dj} \delta K_j \right\rangle_v \end{aligned} \quad (1)$$

97 In the preceding equation, $\partial_\parallel = \frac{P_\parallel}{qR} \partial_\theta$, $P_\parallel = \frac{\kappa_B a r R}{J_B B}$, and θ is the extended poloidal

98 angle in the ballooning representation, $\kappa_\perp = \frac{k_\perp}{k_\theta}$ with $k_\theta = \frac{nq}{r}$, $\omega_A = \frac{v_A}{qR}$ is Alfvén

99 frequency, $\omega_{*pi} = \frac{\mathbf{k} \times \mathbf{b}}{\Omega_{ci} m_i} \cdot \nabla p_i$ is the ion diamagnetic frequency with Ω_{ci} the ion

100 cyclotron frequency, $\alpha = -Rq^2 \beta'$ with $\beta = 8\pi p_i / B^2$, $\langle \dots \rangle_v \equiv \int \dots d^3v$ is the
101 integration over velocity space, q_j is the charge for the particle species j ,

102 $J_0(k_\perp \rho_j)$ is the zeroth order first kind Bessel function with $\rho_j = \frac{v_j}{\Omega_{cj}}$ the Larmor

103 radius, and $\omega_{dj} = \mathbf{k} \cdot \mathbf{b} \times (\mu B + v_\parallel^2) \nabla B / \Omega_{cj}$ is the drift frequency for the particle

104 species j . We further note that the left-hand side of the preceding equation is due
105 to fluid contribution, including field line bending term $\partial_\theta \kappa_\perp^2 \partial_\theta \delta\psi$, inertial term

106 $\frac{1}{P_\parallel^2} \frac{\omega(\omega - \omega_{*pi})}{\omega_A^2} \kappa_\perp^2 \delta\psi$ and ballooning interchange term $\frac{1}{P_\parallel^2} \alpha g \delta\psi$. The right-hand

107 side is due to kinetic compression (KC) of plasmas, which could come from
108 energetic particles or thermal particles.

109 The gyrocenter distribution function δK_j could be acquired by solving the
110 linearized collisionless electromagnetic gyrokinetic equation:

$$\left(\frac{P_\parallel}{qR} \partial_\theta - i\omega + i\omega_d \right) \delta K_j = i \frac{q_j}{m_j} Q F_{0j} \frac{\omega_{dj}}{\omega} J_0(k_\perp \rho_j) \delta\psi, \quad (2)$$

111 where $Q F_{0j} = (\omega \partial_E + \hat{\omega}_{*j}) F_{0j}$ is free energy provided by the phase space

112 gradient of the equilibrium distribution function F_{0j} , with $E = \frac{1}{2} v^2$ and $\hat{\omega}_{*j} =$

113 $\frac{\mathbf{k} \times \mathbf{b}}{\Omega_{cj}} \cdot \nabla \ln F_{0j}$.

114 In the ballooning representation, the vorticity equation of Eq. (1) can be
 115 further organized as a Schrödinger-like form

$$\left[\partial_\theta^2 + \frac{1}{P_\parallel^2} \frac{\omega(\omega - \omega_{*pi})}{\omega_A^2} + V(\theta) \right] \Psi = \sum_j \left\langle \frac{4\pi q_j}{k_\theta^2 c^2 P_\parallel^2 \kappa_\perp} J_0(k_\perp \rho_j) \omega \omega_{dj} \delta K_j \right\rangle_\nu, \quad (3)$$

116 where $V(\theta) = \frac{1}{P_\parallel^2} \frac{\alpha g}{\kappa_\perp^2} - \frac{1}{\kappa_\perp} \frac{\partial^2 \kappa_\perp}{\partial \theta^2}$ is the effective potential well and $\Psi = \kappa_\perp \delta \psi$. To
 117 calculate accurately the eigen frequency ω of the preceding equation, we need to
 118 properly deal with the asymptotic boundary condition in the inertial regime where
 119 the parallel coordinate $\theta \gg 1$. The generalized form of the asymptotic vorticity
 120 equation can be written as

$$(\partial_\theta^2 + \Lambda^2) \Psi = 0 \quad (4)$$

121 The asymptotic behaviour of Ψ can be derived by the Floquet theory as $\theta \gg$
 122 1:

$$\lim_{\theta \rightarrow \infty} \Psi = P(\theta) e^{i\nu|\theta|}, \quad (5)$$

123 where $P(\theta)$ is a fast oscillating function with 2π periodicity and $\Lambda = -i \frac{1}{P} \frac{\partial P}{\partial \theta} +$
 124 ν is the inertial term in the GFLDR theory.[23,24]

125 The kinetic compression term of Eq. (3) involves a multi-dimensional integral
 126 for δK_j , which can be solved by the gyrokinetic equation Eq. (2). For studying BAE
 127 instability, we need only consider circulating particle contribution, and thus the
 128 gyrokinetic equation can be integrated directly in the ballooning space:

$$\begin{aligned} \delta K_j(\theta, \hat{\sigma}, \lambda, E) = & \hat{\sigma} \int_{-\hat{\sigma}\infty}^{\theta} \exp \left[i \hat{\sigma} \text{sign}(Im\omega) \int_\theta^x \frac{-\omega + \omega_{dj}}{P_\parallel |v_\parallel|} dx \right] \\ & \times i \frac{q_j}{m_j} \frac{qR}{|v_\parallel| P_\parallel} QF_{0j} \frac{\omega_{dj}(x)}{\omega} J_0 \frac{\Psi(x)}{\kappa_\perp(x)} dx \end{aligned} \quad (6)$$

129 where $\hat{\sigma} = \frac{v_\parallel}{|v_\parallel|} = \pm 1$ represents co- and counter- direction for the parallel
 130 velocity, $\lambda = \frac{\mu B_0}{E}$ is the pitch angle variable. Hence, the kinetic compression term
 131 has the following integral form

$$\begin{aligned}
KC &\equiv \kappa_{\perp}^{-1} \left\langle \frac{4\pi q_j q^2 R^2}{k_{\theta}^2 c^2 P_{\parallel}} J_0(k_{\perp} \rho_j) \omega \omega_{dj} \delta K_j \right\rangle_v \\
&= \frac{4\pi q_j q^2 R^2}{k_{\theta}^2 c^2 P_{\parallel}^2} \\
&\times \int_0^{+\infty} dE \int_0^1 d\lambda \int_{-\infty}^{+\infty} dx \frac{2\pi E \omega_{dj}(\theta)}{|v_{\parallel}| \kappa_{\perp}(\theta)} J_0 i \frac{q_j}{m_j} \frac{qR}{|v_{\parallel}| P_{\parallel}} Q F_{0j} \\
&\times \exp \left[i \text{sign}(Im\omega(\theta - x)) \int_{\theta}^x dx q R \frac{-\omega + \omega_{dj}(x)}{|v_{\parallel}| P_{\parallel}} \right] \frac{\omega_{dj}(x)}{\kappa_{\perp}(x)} J_0 \Psi(x)
\end{aligned} \tag{7}$$

132 The computational model for the DAEPS code consists of Eqs. (3), (5) & (7) for
133 the purpose of calculating BAE, which is suitable for arbitrary equilibrium
134 magnetic field. The original DAEPS code is based on a simplify equilibrium field
135 model with concircular cross section. In this paper, we modify the original
136 equilibrium to incorporate the important shaping factor of elongation by updating
137 geometric coefficients such as κ_{\perp} and g functions in the model equations. The
138 shaped equilibrium magnetic field model is introduced in the following section.

139

140 B. Equilibrium Model with Elongation

141 In order to study the elongation effect on the BAE instability in a tokamak, a
142 local large aspect-ratio plasma equilibrium with shifted elongated flux surfaces is
143 used in this paper. These elongated flux surfaces can be defined by the following
144 equations for their (R, Z) coordinates:

$$\begin{cases} R = 1 + r \cos \theta_g - \Delta(r) \\ Z = \kappa r \sin \theta_g \end{cases} \tag{8}$$

145 where κ is the elongation factor, θ_g is the geometric poloidal angle, r is a radial
146 variable and a flux label and the length are normalized by major radius R_0 . This
147 model equilibrium is similar to the Miller equilibrium, and includes Shafranov
148 shift $\Delta(r)$. In this model, the flux surface is defined by the radial variable r and
149 the magnetic flux surfaces for different values of elongation are exhibited in Fig .1.

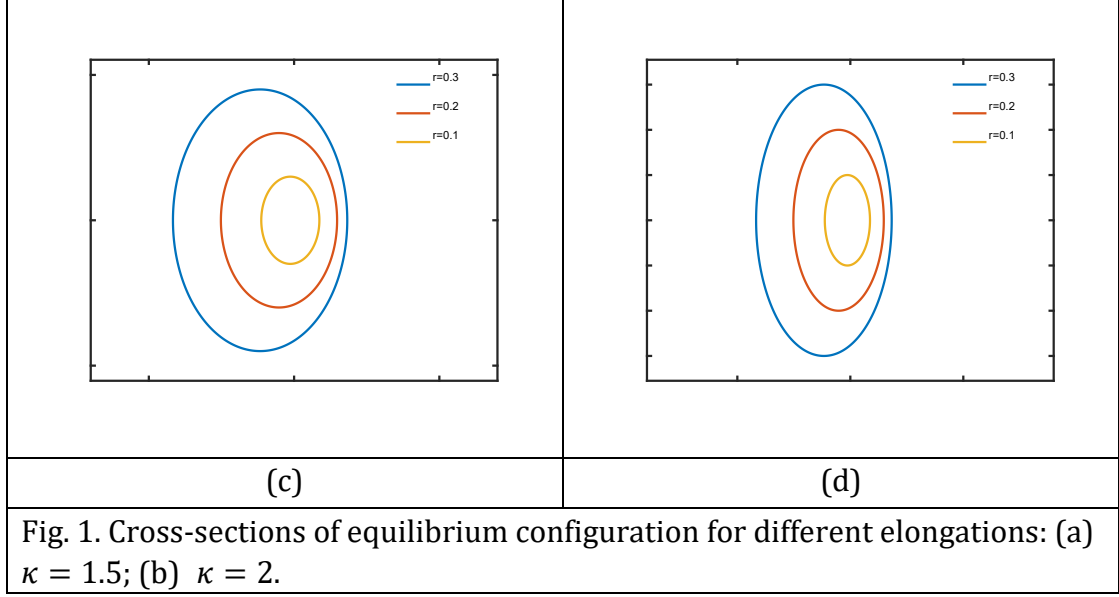
150

The magnetic field associated with this equilibrium model is of the form

$$\mathbf{B} = B_a \nabla \zeta_g + B_a \frac{\kappa r}{q} \nabla \zeta_g \times \nabla r \tag{9}$$

151

where ζ_g is the geometric toroidal angle, B_a is the on-axis magnetic field.



152 To the order of $O(r)$, the Jacobian $J_g = (\nabla r_g \cdot \nabla \theta_g \times \nabla \zeta_g)^{-1}$ could be calculated
 153 as

$$J_g = \kappa r R (1 - \Delta' \cos \theta_g) \quad (10)$$

154 In the DAEPS code, the normalized pressure gradient $\alpha = -q^2 \frac{2\mu_0 P'}{B_0^2}$ are
 155 actually used to calculate linear instability instead of the Shafranov shift $\Delta(r)$.
 156 Thus, we proceed to discuss the relationship between the physical quantities
 157 (α, Δ) and the physical quantities (s, α) in the conventional $s - \alpha$ model. For
 158 this purpose, we resort to the original Grad-Shafranov (G-S) equation.

$$\nabla \cdot \left(\frac{\nabla \psi_p}{R^2} \right) = -\mu_0 \frac{dP}{d\psi_p} - \frac{F}{R^2} \frac{dF}{d\psi_p}, \quad (11)$$

159 where $F = B_\phi R$ represents the poloidal current. In the $s - \alpha$ model for circular
 160 flux surfaces, we can solve this preceding equation by perturbation method
 161 according to the smallness of r/R_0 . To the lowest order, the preceding G-S
 162 equation can be turned into the following radial force balance equation[25]:

$$2\mu_0 \frac{P'}{B_0^2} + \frac{1}{q^2} \left[\left(3 - 2 \frac{q'r}{q} \right) \Delta' - r + r\Delta'' \right] = 0 \quad (12)$$

163 From Eq. (13), ignoring the $O(r)$ term, we can find the relationship between
 164 the normalized pressure gradient α and Shafranov shift $\Delta(r)$: $r(\Delta' + r) = \alpha$.
 165 However, when the elongation effect is considered, there will be extra shaping
 166 factors in the G-S equation. Thus, it is not feasible to obtain a pure radial force
 167 balance equation.

168 In the magnetic coordinates (r, θ_g, ζ_g) , Eq. (11) can be rewritten as

$$\begin{aligned} & \frac{\partial J_g}{\partial r} \frac{J_g}{R^2} g^{rr} \frac{\partial \psi_p}{\partial r} + \frac{\partial J_g}{\partial r} \frac{J_g}{R^2} g^{r\theta_g} \frac{\partial \psi_p}{\partial \theta_g} + \frac{\partial J_g}{\partial \theta_g} \frac{J_g}{R^2} g^{\theta_g r} \frac{\partial \psi_p}{\partial r} \\ & + \frac{\partial J_g}{\partial \theta_g} \frac{J_g}{R^2} g^{\theta_g r} \frac{\partial \psi_p}{\partial \theta_g} = \frac{J}{R^2} [-\mu_0 R^2 P'(\psi_p) - FF'(\psi_p)] \end{aligned} \quad (13)$$

169 where the geometric tensor coefficients can be found as: $g^{rr} = \frac{\kappa^2 \cos^2 \theta_g + \sin^2 \theta_g}{\kappa^2 (1 - \Delta' \cos \theta_g)^2}$,
 170 $g^{r\theta_g} = \frac{(-\kappa^2 + 1) \sin \theta_g \cos \theta_g - \Delta' \sin \theta_g}{\kappa^2 (1 - \Delta' \cos \theta_g)^2}$, $g^{\theta_g \theta_g} = \frac{\kappa^2 \sin^2 \theta_g + \cos^2 \theta_g}{\kappa^2 (1 - \Delta' \cos \theta_g)^2}$. The poloidal magnetic
 171 flux ψ_p can be expanded as

$$\psi_p = \psi_0 + \psi_1 (r - r_0) + \psi_2 (r - r_0)^2 + \dots \quad (14)$$

172 Substituting Eq. (11) in the Eq. (13), we can obtain ψ_2 as

$$\begin{aligned} \psi_2 = & \frac{D^2}{2r^2 A} [-\mu_0 R^2 P'(\psi_p) - FF'(\psi_p)] - \frac{\partial}{\partial \theta_g} \left(\frac{C}{DR} \right) \times \frac{DR \psi_1}{2rA} - \\ & \frac{\partial}{\partial r} \left(\frac{r^2 A}{DR} \right) \times \frac{\psi_1 DR}{2r^2 A}, \end{aligned} \quad (15)$$

173 where the constants are defined as: $A = \kappa^2 \cos^2 \theta_g + \sin^2 \theta_g$, $D = \kappa r (1 -$
 174 $\Delta' \cos \theta_g)$, $C = (1 - \kappa^2) \sin \theta_g \cos \theta_g - \Delta' \sin \theta_g$, and the first order of the flux
 175 surface expansion is found to be $\psi_1 = \frac{\kappa B_a r}{q}$.

176 Then we make the following choice: $\psi_p(r, \theta_g = 0) = \psi_p(r, \theta_g = \pi)$, which
 177 means, for a particular magnetic surface, the same radial coordinate ψ_p can be
 178 shifted horizontally to be tangent to this specific magnetic surface on both high
 179 and low field sides [26]. Then the relationship between Δ'' and α can be found
 180 by using the expansion in Eq. (14):

$$r(\Delta' + r)' = \frac{\alpha}{\kappa^2} \quad (16)$$

181 So far, we have finished adding elongation factor in the $s - \alpha$ equilibrium field
 182 model.

183 C. Geometric Modifications with Boozer Coordinates in Ballooning Space

184 Next we show the key geometric modifications to the gyrokinetic equation and
 185 vorticity equation when considering elongation in the equilibrium model. As is
 186 shown in Eq. (5) & (7), the Boozer coordinates are used for the gyrokinetic model
 187 and ballooning representation are used for the electromagnetic perturbations. The
 188 Boozer coordinate is not only a straight field line coordinate, but also satisfies
 189 $J_B = f(\psi_p)/B^2$. Accurate to $O(r)$, the Jacobian of the Boozer coordinates J_B can
 190 be obtained from Eq. (17)

$$J_B = (\nabla \psi_p \times \nabla \theta_B \cdot \nabla \zeta_B)^{-1} = \kappa r R_0 (1 + 2r \cos \theta_g) \quad (17)$$

191 Using this Boozer Jacobian, the relationship between the Boozer coordinates
 192 (r, θ_B, ζ_B) and magnetic coordinates (r, θ_g, ζ_g) used in the preceding section can
 193 be obtained:

$$\theta_B = \theta_g - (\Delta' + r) \sin \theta_g, \quad (18)$$

194 and

$$\zeta_B = \zeta_g - \nu(r, \theta_g) \quad (19)$$

195 where ν is a function of $O(r^2)$, which could be ignored in our model. In order to
 196 implement the shaping factor in the gyrokinetic equation and vorticity equation,
 197 we need to examine how the differential operators in these equations change with
 198 the shaping factor in the Boozer coordinates. The gradient operator in the Boozer
 199 coordinates can be written as $\nabla f = \nabla r \partial_r f + \nabla \theta_B \partial_{\theta_B} f + \nabla \zeta \partial_{\zeta} f$, which can be
 200 further expressed in the ballooning representation:[27]

$$\nabla f(r, \theta_B, \zeta) \rightarrow [\nabla \theta (-inq + \partial_\theta) + \nabla r (-inq' \theta + \partial_r) + in \nabla \zeta] \hat{f}(\vartheta) \quad (20)$$

201 With the preceding gradient operator and the equilibrium constraint in Eq.
 202 (16), we can find the quotient $\left(\frac{k_\perp}{k_\theta}\right)^2$ and magnetic drift term $\frac{\vec{B}}{B} \times \nabla \ln B \cdot \mathbf{k}$ in the
 203 ballooning representation:

$$\begin{aligned} \kappa_\perp^2 = \left(\frac{k_\perp}{k_\theta}\right)^2 &\rightarrow 1 + \left(s\theta - \frac{\alpha}{\kappa^2} \sin \theta\right)^2 \\ &+ \frac{1 - \kappa^2}{\kappa^2} \left[\cos \theta + \left(s\theta - \frac{\alpha}{\kappa^2} \sin \theta\right) \sin \theta\right]^2 \end{aligned} \quad (21)$$

204

$$\frac{\vec{B}}{B} \times \nabla \ln B \cdot \mathbf{k} \rightarrow \frac{k_\theta \left[\cos \theta + \left(s\theta - \frac{\alpha}{\kappa^2} \sin \theta\right) \sin \theta\right]}{\kappa} \quad (22)$$

205

$$P_\parallel = 1 \rightarrow \partial_\parallel = \frac{1}{qR} \partial_\theta \quad (23)$$

206

207 Using these expressions, the forms of g , κ_\perp and other relevant physical
 208 quantities in Eqs. (3) & (7) can be calculated for the shaped plasma defined in Eq.
 209 (11) and implemented in the GTC code, as will be shown in next section.

210

211 III. DAEPS calculation of BAE instability with elongation

212 The coupling between shear Alfvén waves (SAW) and sound wave (SW) caused
 213 by the plasma compressibility could induce a gap for Alfvén continuum spectrum,
 214 where the Beta induced Alfvén Eigenmode (BAE) is located. Generally speaking,
 215 BAE can be excited either by thermal ions or by energetic particles through wave-
 216 particle resonance. In this paper, we focus our study on the BAE mode excited by
 217 the thermal ions. The parallel mode structure of BAE is rather smooth, i.e., the
 218 BAE's mode structure in the ballooning representation changes slowly with the

219 extended poloidal angle θ , which makes the ideal MHD assumption applicable, i.e.,
 220 the parallel electric field $\delta E_{\parallel} \approx 0$.

221 The DAEPS code can calculate the BAE/KBM instability by invoking either a
 222 simple semi-analytic method or a more complex numerical method to integrate
 223 kinetic compression (KC) term: the simple method or reduced kinetic compression
 224 (rkC) method is based on a drift center transformation to integrate the KC term,
 225 which is fast computationally but less accurate; and the more complex method or
 226 complete kinetic compression (cKC) method is based on a brute force numerical
 227 integration of the KC term, which is more accurate but computationally much more
 228 expensive. Thus, the rkC method could be used not only to compute the linear
 229 eigenvalues in a semi-quantitative sense, but also to provide an initial guess for the
 230 eigen frequency ω , asymptotic behavior Λ , and help set up simulation domain
 231 and grid size for the cKC method. Moreover, the rkC method can also be used to
 232 analyze the physical mechanism because of its simplicity.

233 In the rkC method, the following drift center transformation is used to simplify
 234 the process of solving the gyrokinetic equation [16,22,28]. Firstly we make the
 235 following forward transformation to change the gyrocenter distribution δK_j to
 236 the drift center distribution δK_{dj} [28]:

$$\delta K_{dj} = \delta K_j \exp\left(\int^{\theta} i \frac{\omega_{dj}}{\omega_{tj}} d\theta\right). \quad (24)$$

237 Then the drift center distribution function δK_{dj} satisfies the following
 238 kinetic equation:

$$\left(\hat{\sigma} \omega_{tj} \partial_{\theta} - i\omega\right) \delta K_{dj} = i \frac{q_j}{m_j} Q F_{0j} \frac{\Omega_{dj}}{\omega} J_0 \frac{g}{\kappa_{\perp}} \delta \Psi \exp\left(\int^{\theta} i k_{\perp} \rho_{dj} \frac{g}{\kappa_{\perp}} d\theta\right) \quad (25)$$

239 where $\rho_{dj} = qv/\omega_{ci}$, $\Omega_{dj} = \frac{\omega_{dj}}{g}$. As we have derived for shaped equilibrium, the
 240 geometric function g/κ_{\perp} in the preceding equation has the following form in the
 241 ballooning space:

$$\begin{aligned} & \frac{g}{\kappa_{\perp}} \\ &= \frac{\left[\cos \theta + \left(s\theta - \frac{\alpha}{\kappa^2} \sin \theta\right) \sin \theta\right]}{\kappa} \\ &= \frac{\left[\cos \theta + \left(s\theta - \frac{\alpha}{\kappa^2} \sin \theta\right) \sin \theta\right]}{\sqrt{1 + \left(s\theta - \frac{\alpha}{\kappa^2} \sin \theta\right)^2 + \frac{1 - \kappa^2}{\kappa^2} \left[\cos \theta + \left(s\theta - \frac{\alpha}{\kappa^2} \sin \theta\right) \sin \theta\right]^2}} \end{aligned} \quad (26)$$

242
 243 This expression is too complex to be integrated analytically over θ . However, in
 244 the inertial region ($\theta \gg 1$) where the kinetic response is non-negligible, the
 245 ballooning angle integration in Eq. (25) can be carried out approximately. Since $\frac{g}{\kappa_{\perp}}$
 246 is an odd function of θ as $\theta \gg 1$, the expression in Eq. (26) can be expanded in
 247 the following Fourier series:

$$\frac{g}{\kappa_{\perp}} = G_1 \sin \theta + G_3 \sin 3\theta + \dots \quad (27)$$

248 where G_1 represents the first Fourier component in the poloidal angle expansion
 249 for the geodesic curvature coupled with the elongation effect. It is found that the
 250 G_1 term should be just sufficient to the requisite accuracy because G_1 is much
 251 larger than the rest expansion coefficients such as G_3 . And then it is calculated
 252 that G_1 takes the following form:

$$G_1 = \frac{1}{\pi} \int_0^{2\pi} \frac{\sin^2 \theta}{\sqrt{\kappa^2 \cos^2 \theta + \sin^2 \theta}} d\theta = \frac{2}{\pi(\kappa^2 - 1)} \{ \kappa^2 K(1 - \kappa^2) - E(1 - \kappa^2) + \kappa \left[K \left(1 - \frac{1}{\kappa^2} \right) - E \left(1 - \frac{1}{\kappa^2} \right) \right] \} \quad (28)$$

253 Therefore, the gyrokinetic equation for drift centre distribution becomes

$$\begin{aligned} & (\hat{\sigma} \omega_{tj} \partial_{\theta} - i\omega) \delta K_{dj} \\ & = i \frac{q_j}{m_j} Q F_{0j} \frac{\Omega_{dj}}{\omega} J_0 G_1 \sin \theta \delta \Psi \exp(-ik_{\perp} \rho_{dj} G_1 \cos \theta) \end{aligned} \quad (29)$$

254 The exponential function in the preceding equation can be expanded in the Bessel
 255 series, $e^{ix \cos \theta} = \sum_n i^n J_n(x) e^{in\theta}$. In general, only the $n = 1$ term needs to be
 256 considered, thus the kinetic drift centre response can be found as

$$\delta K_{dj} = i \frac{q_j}{m_j} Q F_{0j} \frac{\Omega_{dj}}{\omega} J_{0j} \delta \Psi \frac{J_1(G_1 k_{\perp} \rho_{di})}{k_{\perp} \rho_{di}} \left(\frac{e^{i\theta} - e^{-i\theta}}{\omega - \omega_{ti}} \right) \quad (30)$$

257 Use the pull-back transformation for the drift motion and insert the proceeding
 258 expression in Eq. (7), we can obtain the following form for the kinetic compression:

$$KC = \left\langle \frac{4\pi q_j^2 q^2 R^2}{k_{\theta}^2 c^2 m_j} Q F_j \Omega_{dj}^2 \delta \Psi \frac{J_{0i}^2 J_1^2(G_1 k_{\perp} \rho_{di})}{(k_{\perp} \rho_{di})^2} \left(\frac{e^{2i\theta} + e^{-2i\theta} - 2}{\omega - \omega_{ti}} \right) \right\rangle \quad (31)$$

259 In Eq. (31), ω_{ti} is the transit frequency. the $J_n(k_{\perp} \rho_j)$ is the n th order Bessel
 260 function of the first kind. In the long wavelength limit, we can obtain:

$$KC = \left\langle \frac{4\pi q_j^2 q^2 R^2}{k_{\theta}^2 c^2 m_j} Q F_j \Omega_{dj}^2 \delta \Psi \frac{1}{\omega - \omega_{ti}} G_1^2 \sin^2 \theta \right\rangle \quad (32)$$

261 According to the theory[12], both BAE and KBM can be driven by η_i . Below
 262 some critical value of η_{ic} , the KBM is the most unstable mode; and above η_{ic} , the
 263 KBM is coupled with the BAE mode. The traditional calculation of the BAE/KBM
 264 instability by the DAEPS code is based on the concircular flux surface model[16].
 265 Here we show how the BAE/KBM growth rate varies with elongation of the
 266 magnetic flux surface, as is shown in Fig. 2, where the data is calculated by the
 267 DAEPS code with plasma parameters $\beta_i = 0.01$, $q = 1.5$, $\omega_{*ni} = \omega_{Ti}$, and $\eta_i =$
 268 1, 1.2, 1.5 .

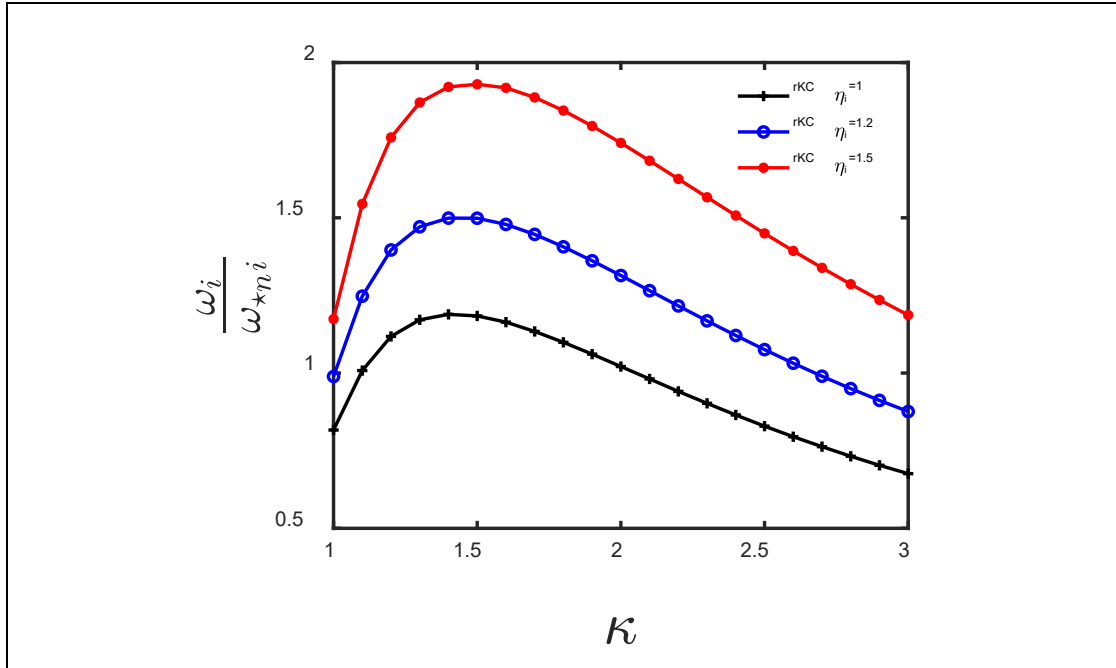


Fig. 2. Linear growth rate or $Im\Omega = \omega_i/\omega_{*ni}$ of BAE instability varies with elongation factor κ for various η_i .

269 As can be seen from Fig .2, the growth rate or $Im(\Omega)$ with $\Omega \equiv \omega/\omega_{*ni}$ of
 270 the BAE mode firstly increases with elongation to a maximum value as the
 271 elongation $\kappa \sim 1.5$, and then it decreases with the elongation monotonically. In this
 272 case, we note that the pressure gradient α increases with η_i , e.g. $\alpha =$
 273 $0.45, 0.495, 0.5625$ when $\eta_i = 1, 1.2, 1.5$, respectively. Fig. 2 also shows that, for
 274 the same elongation κ , the growth rate $Im\Omega$ increases with η_i and thus
 275 increases with α , which is consistent with the BAE theory[16,19].

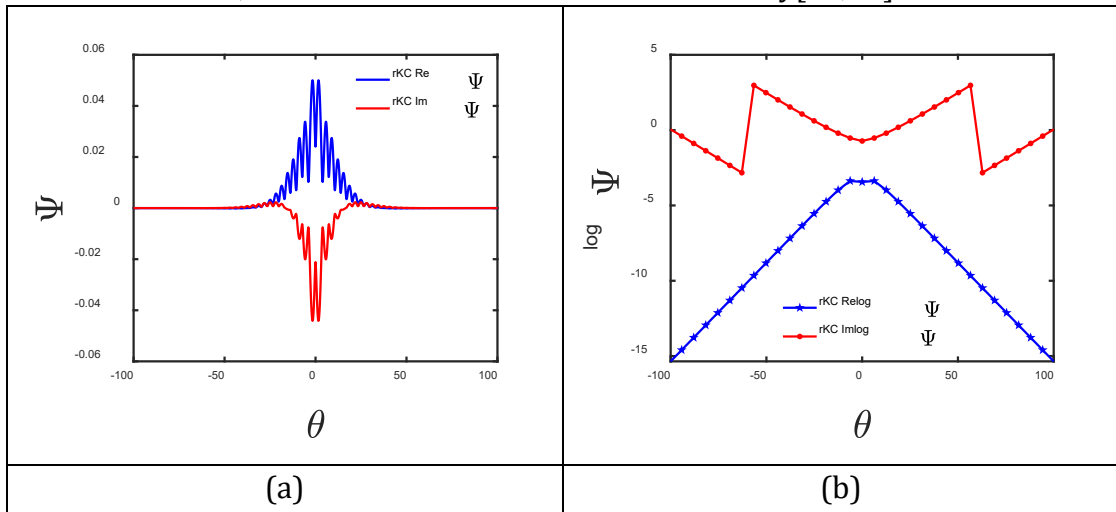


Fig. 3. BAE mode structure for elongated equilibrium with $\kappa = 3$ and $\eta_i = 1$ using rKC integration method for the KC term. (a) linear scale; (b) logarithmic scale.

276 Figure. 3 exhibits parallel mode structures of BAE for $\kappa = 3$ and $\eta_i = 1$ using
 277 reduced integration method for the kinetic compression (KC) term. This reduced
 278 kinetic compression (rKC) method is semi-analytic and much faster than the brute

279 force integration method or complete kinetic compression (cKC) method, which
 280 are both implemented in the DAEPS code. The DAEPS code requires that the
 281 simulation domain should be wide enough to cover the non-vanishing asymptotic
 282 mode structure for the outgoing wave boundary condition, and the grid size should
 283 be small enough to achieve numerical convergence, e.g., $\Delta\theta < 0.2$. It can be seen
 284 from Fig .3(a) that the widths of different mode structures are in the range of
 285 $[-50, 50]$, which is much narrower than the simulation domain. The fast-spatial
 286 oscillation component of the mode in Fig3. (a) is caused by $P(\theta)$, which is an
 287 oscillatory function with a period of 2π . According to the Floquet theory and Eq.
 288 (5), the logarithm of Ψ varies linearly with the ballooning angle θ in the inertial
 289 region, which suggests that there is negligible numerical error generated by the
 290 numerical asymptotic matching process. Thus, the mode structure in the ideal
 291 region can hardly be distorted by the inertial region computation. Using this
 292 asymptotic matching process for the boundary condition, we can significantly
 293 narrow down the simulation domain in the inertial region while maintaining high
 294 computational accuracy. For example, the simulation domain is set as $[-100, 100]$
 295 for the calculation in Fig3. (a), and the grid size is set as $\Delta\theta = 0.05\pi$. With these
 296 settings, we can use cKC method to calculate the eigen frequency for the BAE mode.

297 With the parallel mode structure of BAE in the ballooning representation, the
 298 3-dimensional mode structure could be drawn in real space using the following
 299 transform:

$$\delta\psi(r, \theta, \zeta) = \sum_{n,m} e^{i(n\zeta - m\theta)} \int e^{-i(nq - m)\theta'} \delta\psi_n(r, \theta') d\theta', \quad (33)$$

300 where θ' is the ballooning angle and θ is the angle in the real space. To mimic the
 301 global radial variance, we can artificially modulate the mode function with an
 302 envelope function $M(r)$, i.e. a super Gaussian function, defined as the following:

$$M(r) = \text{Exp}\left[-\frac{(r-r_c)^4}{\Delta r^4}\right], \quad (34)$$

303 where we choose $r_c = a/2$, $\Delta r = a/2$. The resultant two-dimensional mode
 304 structure is illustrated in Fig. 4, which is similar to the 2D mode structure
 305 calculated by other simulation codes, except the elongation effect.

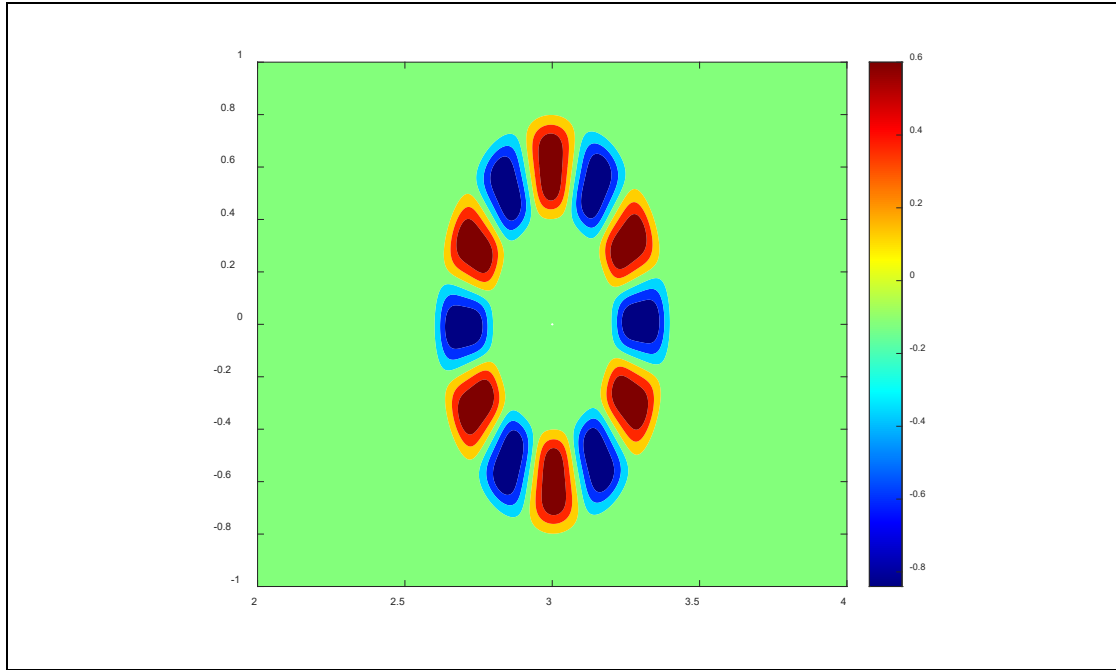


Fig. 4. 2D mode structure of BAE in poloidal plane with $\kappa = 2..$

306

307

IV. Theoretical analysis for elongation effect on BAE

308

309

310

311

312

313

314

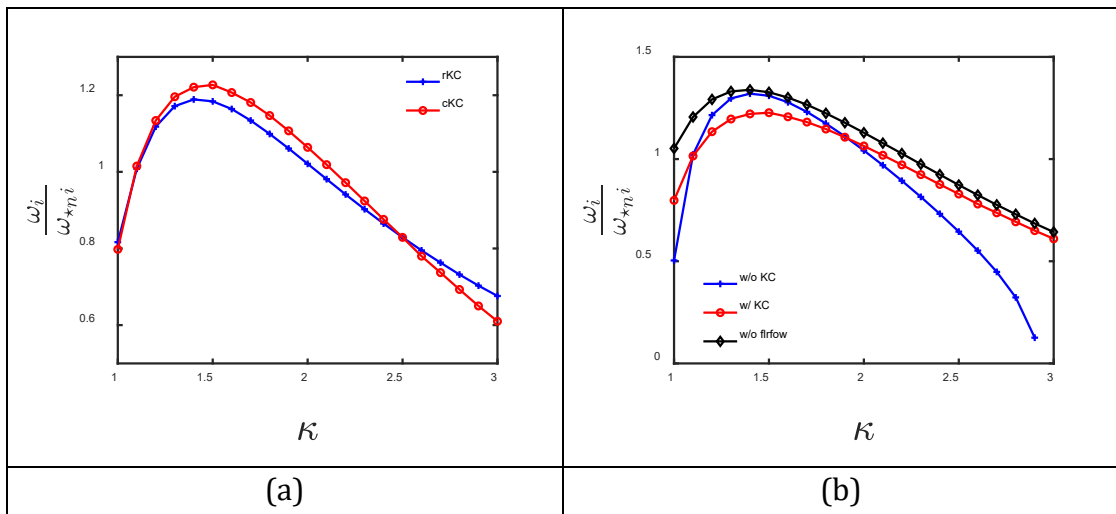
315

316

317

318

In this section, we provide detailed theoretical analysis for the elongation effect on the BAE instability. First we show how the BAE growth rates varies with elongation κ using the DAEPS code, as is demonstrated in Fig. 5, where the result from the rKC method is compared to the completed KC term (cKC) method, with the same parameters as in the $\eta_i = 1$ case in Fig. 2. The red circle line is the growth rate $Im\Omega$ calculated by cKC while the blue plus line is the growth rate or $Im\Omega$ calculated by reduced KC term (rKC). The growth rate from rKC agrees well quantitatively with that from cKC, justifying the use of the simplification method of rKC. This agreement provides a solid basis for investigating the instability BAE using the formula in Eq. (32).



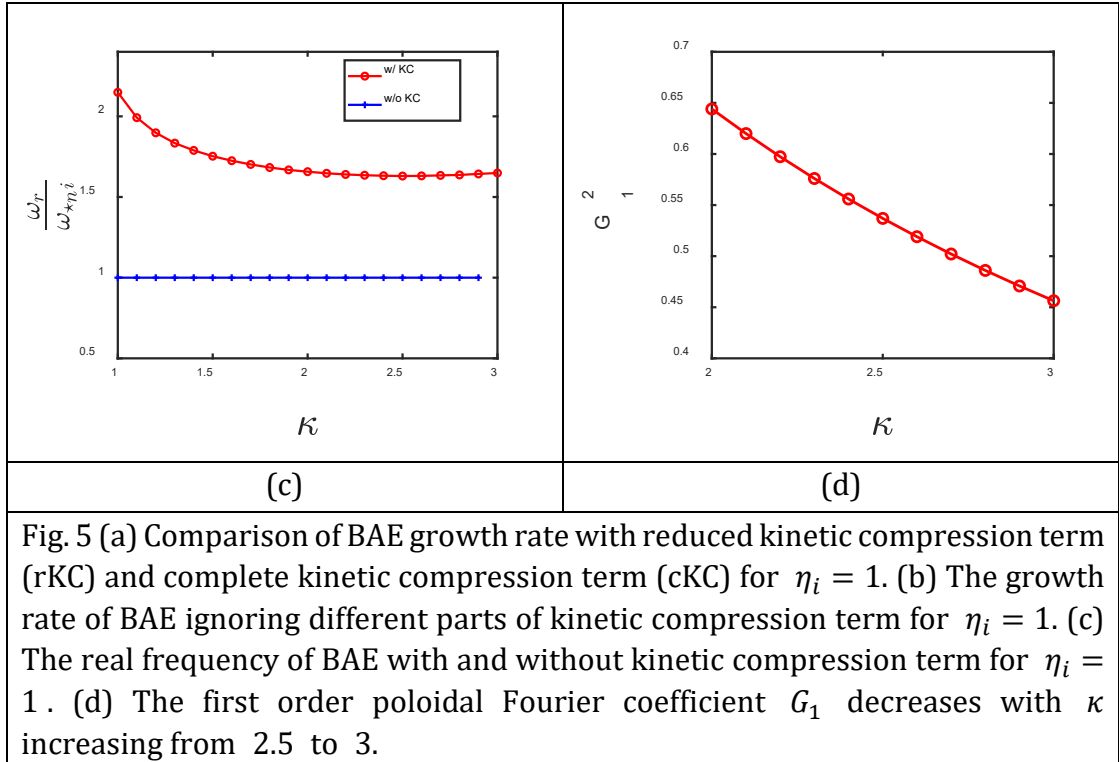


Fig. 5 (a) Comparison of BAE growth rate with reduced kinetic compression term (rKC) and complete kinetic compression term (cKC) for $\eta_i = 1$. (b) The growth rate of BAE ignoring different parts of kinetic compression term for $\eta_i = 1$. (c) The real frequency of BAE with and without kinetic compression term for $\eta_i = 1$. (d) The first order poloidal Fourier coefficient G_1 decreases with κ increasing from 2.5 to 3.

319 As is shown in Fig. 5(a), the growth rate of BAE firstly increases with the
 320 elongation κ , reaches a maximum, and then decreases. In order to analyze kinetic
 321 and fluid/MHD contributions to the growth rate of BAE/KBM, we artificially
 322 remove the kinetic compression term and recalculate the growth rate. As is shown
 323 in Fig. 5(b), the red circle line is obtained from the cKC method, the blue plus line
 324 is obtained by removing the KC term, and the black diamond line is calculated
 325 without the FLR and FOW effect. The trend of growth rate varying with κ without
 326 the kinetic compression term (KC) or δW_k is essentially the same as the original
 327 trend. And there exists a notable difference between the growth rates with and
 328 without the KC term when the elongation $\kappa > 2.5$. In this strongly elongated
 329 region, the BAE growth rate with only the MHD effect decreases rapidly with κ
 330 increasing, and it nearly disappears at $\kappa = 3$. However, the stability results with
 331 the KC term shows that the BAE is still unstable, and decreases gradually around
 332 $\kappa = 3$. Based on these observations, it is then conjectured that the trend of the BAE
 333 instability is mainly related to the MHD effect around the turning point ($\kappa \approx 1.5$),
 334 and the instability in the strongly elongated region $\kappa > 2.5$ is caused by the
 335 kinetic effect, such as wave-particle resonance.

336 To justify our viewpoint, the kinetic contribution to the potential energy
 337 δW_k , and the fluid contribution to the potential energy δW_f needs to be examined
 338 as κ increases. δW_k can be calculated by $\langle \delta\psi | KC | \delta\psi \rangle$, where $\delta\psi$ is the
 339 normalized eigenfunctions, and δW_f can be acquired by $\langle \delta\psi | W | \delta\psi \rangle$, where W
 340 contains the Schrödinger potential well term (interchange term) and field line
 341 bending term. Therefore, we could rewrite the vorticity equation as

$$C\omega + D\omega^2 - i\Lambda B - \delta W_f - \delta W_k = 0 \quad (35)$$

342 Similarly, $C = \left\langle \delta\psi \left| \frac{-\omega_{*pi}}{\omega_A^2} \right| \delta\psi \right\rangle$, $D = \left\langle \delta\psi \left| \frac{1}{\omega_A^2} \right| \delta\psi \right\rangle$, and $B = \langle \delta\psi | B.C. | \delta\psi \rangle$ is
 343 the boundary condition term, which is much smaller than δW_f and δW_k for this
 344 case. Thus Eq. (35) is a quadratic equation about ω and its solution can be
 345 expressed as

$$\omega = \frac{-C/2 \pm \sqrt{\frac{C^2}{4} + (\delta W_f + \delta W_k)}}{D} \quad (36)$$

346 To verify the previous conjecture, we could solve the preceding eigen equation
 347 by ignoring $Im\delta W_k$, and compare the resultant eigenvalue ω . As is shown in Fig.
 348 6 (a), the trend of the growth rate is almost the same in both cases when $\kappa < 2$,
 349 which suggests a fluid instability of reactive type. But in the region $\kappa > 2.5$, there
 350 is a noticeable difference: when the whole kinetic compression term is considered,
 351 the growth rate decreases gradually with κ ; whereas when $Im\delta W_k$ is ignored,
 352 the growth rate decays rapidly. Therefore, $Im\delta W_k$ is the main cause of the
 353 instability of BAE in this strongly elongated region. We proceed to verify our
 354 previous conjecture by analyzing the change in the magnitude of various potential
 355 energies in Fig.6 (b). When $1 < \kappa < 2$, the change of δW_k can be considered to
 356 be approximately invariant compared to δW_f . Thus, in this region, the change in
 357 the growth rate is mainly determined by the change in δW_f . When $\kappa > 2.5$, both
 358 δW_f and $Re\delta W_k$ decays towards zero and they tend to cancel each other. In fact,
 359 in this region, $\delta W_f + Re\delta W_k$ can be shown to be much smaller than $Im\delta W_k$ in
 360 Fig. 6(b). This suggests that the instability or linear growth is mainly caused by
 361 $Im\delta W_k$ in this region.

362 As Fig.5 (b) shows, the kinetic contribution δW_k decreases with elongation
 363 κ when $\kappa > 2.5$. The red circle and black diamond lines in Fig. 5 (b) represents
 364 BAE growth rates vs. κ with or without FLR-FOW (finite Larmor radius & finite
 365 orbit width) effects respectively. These two lines are coincident with each other
 366 when $\kappa > 2.5$, which suggests that the FLR or FOW effect has little influence on
 367 the growth rate. Therefore, the kinetic effect in this region is mostly likely due to
 368 wave-particle resonance, which corresponds to $Im\delta W_k$ mathematically and
 369 suggests a dissipative instability.

370 Next we try to analyze why the wave-particle resonance effect decays with
 371 elongation κ increasing in the strongly shaped region. We examine the form of
 372 kinetic compression term with holding off the FLR and FOW effects after
 373 performing the drift center transformation. As Eq. (36) shows, the kinetic
 374 compression term is related to $\frac{1}{\omega - \omega_{ti}}$, i.e., the wave-particle resonance kernel,
 375 and the first order Fourier coefficients G_1 while the first-order expansion is
 376 dominant as shown in Fig4. (a). When $2.5 < \kappa < 3$, the real frequency ω_r is
 377 almost constant in Fig5 (c), suggesting that the resonance position is almost
 378 unchanged in this region. Fig. 5 (d) shows that G_1 decreases with the elongation
 379 κ , which means the first poloidal Fourier coefficient of $\frac{g}{\kappa_\perp}$ decreases with κ . Thus,

380 according to Fig. 5(d) and Eq. (32), we can find that the decrease in δW_k is mainly
 381 caused by the decrease in G_1 . The decrease in the kinetic compression in the
 382 dissipative region is due to the decrease in the projection of geodesic curvature on
 383 the poloidal direction rather than the shift in the wave particle resonance point.

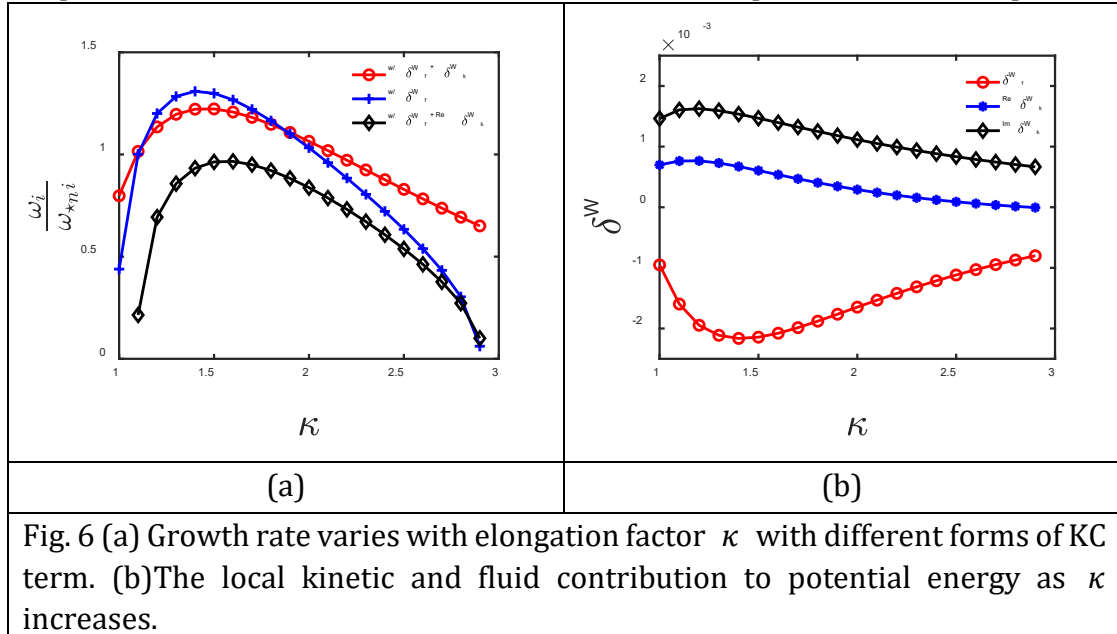


Fig. 6 (a) Growth rate varies with elongation factor κ with different forms of KC term. (b) The local kinetic and fluid contribution to potential energy as κ increases.

384

385 V. CONCLUSION AND DISCUSSION

386 In this paper, we have constructed a local $s - \alpha$ equilibrium model including
 387 the elongation factor and implemented this model in the DAEPS code by modifying
 388 the gyrokinetic equation and vorticity equation using the Boozer coordinates and
 389 Ballooning representation. The elongation effect on the BAE caused by the thermal
 390 ions has been investigated by the DAEPS code with thermal ions as the kinetic
 391 compression. In order to calculate the growth rate of BAE/KBM accurately and
 392 quickly, we have also upgraded the reduced kinetic compression with elongation.
 393 It is discovered that the BAE growth rate first increases, reaches a maximum and
 394 then decreases with elongation. This trend occurs for many different values of η_i
 395 and quite general. We find that, when the shape of cross-section is close to circular,
 396 e.g., $1 < \kappa < 2$, the trend of growth rate is mainly determined by the fluid/MHD
 397 effects, namely the combination of the field line bending term and potential well
 398 term in the vorticity equation, which suggests a reactive instability. However, for
 399 strongly shaped plasma with $\kappa > 2.5$, the growth rate is mainly driven by the
 400 wave-particle resonance embedded in δW_k , which suggests a dissipative instability.
 401 In this dissipative region, the wave-particle resonance effect decreases with the
 402 elongation κ since the dominant poloidal Fourier component of the geodesic
 403 curvature decreases with elongation while the resonant point keeps unchanged.

404 As has been demonstrated, the plasmas shaping effects can introduce many
 405 interesting physics phenomena in drift-Alfvénic instability and turbulence. In the
 406 future, we will introduce more shaping factors in our calculation, e.g., the
 407 triangularity, to investigate how these shaping factors together influence various
 408 drift-Alfvénic instabilities.

409 **Acknowledgement**

410 One of the authors, Yong Xiao, thanks helpful discussions with Professor Liu Chen
411 and Professor Zhihong Lin. This work is supported by NSFC under Grant NO.
412 11975201, National Magnetic Confinement Fusion Energy Research Program of
413 China under Grant No. 2015GB110000.

414

415

416

417 **References**

418 [1] Cheng C, Chen L and Chance M 1985 High- n ideal and resistive shear Alfvén waves in
419 tokamaks *Annals of Physics* **161** 21–47

420 [2] Cheng C Z and Chance M S Low- n shear Alfvén spectra in axisymmetric toroidal
421 plasmas 8

422 [3] Fu G Y and Van Dam J W 1989 Excitation of the toroidicity-induced shear Alfvén
423 eigenmode by fusion alpha particles in an ignited tokamak *Physics of Fluids B: Plasma
424 Physics* **1** 1949–52

425 [4] Wang X, Zonca F and Chen L 2010 Theory and simulation of discrete kinetic beta
426 induced Alfvén eigenmode in tokamak plasmas *Plasma Phys. Control. Fusion* **52** 115005

427 [5] Heidbrink W W, Choi G J, Van Zeeland M A, Austin M E, Degrandchamp G H, Spong D
428 A, Bierwage A, Crocker N A, Du X D, Lauber P, Lin Z and McKee G R 2021 Isotope
429 dependence of beta-induced Alfvén eigenmode (BAE) and low frequency mode (LFM)
430 stability in DIII-D *Nucl. Fusion* **61** 106021

431 [6] Chu M S, Greene J M, Lao L L, Turnbull A D and Chance M S 1992 A numerical study
432 of the high- n shear Alfvén spectrum gap and the high- n gap mode *Physics of Fluids
433 B: Plasma Physics* **4** 3713–21

434 [7] Chen L 2014 Theory of magnetohydrodynamic instabilities excited by energetic
435 particles in tokamaks 5

436 [8] Van Zeeland M, Chrystal C, Du X, Liu D, Thome K, Degrandchamp G, Heidbrink W, Bass
437 E, Collins C, Crocker N, and others 2021 Isotope Impact on Alfvén Eigenmodes and Fast
438 Ion Transport in DIII-D *APS Division of Plasma Physics Meeting Abstracts* vol 2021 pp
439 CP11-073

440 [9] Kusama Y, Kimura H, Ozeki T, Saigusa M, Kramer G J, Oikawa T, Moriyama S, Nemoto
441 M, Fujita T, Tobita K, Fu G Y, Nazikian R and Cheng C Z 1998 Toroidal alfvén eigenmodes
442 driven with ICRF accelerated protons in JT-60U negative shear discharges *Nucl. Fusion*
443 **38** 1215–23

444 [10] Heidbrink W W, Ruskov E, Carolipio E M, Fang J, van Zeeland M A and James R A 1999
445 What is the “beta-induced Alfvén eigenmode?” *Physics of Plasmas* **6** 1147–61

- 446 [11] Zhang H S, Lin Z, Holod I, Wang X, Xiao Y and Zhang W L 2010 Gyrokinetic particle
447 simulation of beta-induced Alfvén eigenmode *Physics of Plasmas* **17** 112505
- 448 [12] Zonca F, Chen L and Santoro R A 1996 Kinetic theory of low-frequency Alfvén modes
449 in tokamaks *Plasma Phys. Control. Fusion* **38** 2011–28
- 450 [13] Briguglio S, Vlad G, Zonca F and Kar C 1995 Hybrid magnetohydrodynamic-gyrokinetic
451 simulation of toroidal Alfvén modes *Physics of Plasmas* **2** 3711–23
- 452 [14] Todo Y and Sato T 1998 Linear and nonlinear particle-magnetohydrodynamic
453 simulations of the toroidal Alfvén eigenmode *Physics of Plasmas* **5** 1321–7
- 454 [15] Anon 2016 Hybrid simulations of Alfvén modes driven by energetic particles *Physics of
455 Plasmas* **23** 122506
- 456 [16] Li Y, Hu S, Zheng W and Xiao Y 2020 Drift Alfvén energetic particle stability with
457 circulating particles *Physics of Plasmas* **27** 062505
- 458 [17] Qi L, Dong J Q, Bierwage A, Lu G and Sheng Z M 2013 Thermal ion effects on kinetic
459 beta-induced Alfvén eigenmodes excited by energetic ions *Physics of Plasmas* **20**
460 032505
- 461 [18] Xie H-S, Lu Z-X and Li B 2018 Kinetic ballooning mode under steep gradient: High
462 order eigenstates and mode structure parity transition *Physics of Plasmas* **25** 072106
- 463 [19] Zonca F, Chen L and Santoro R A 1996 Kinetic theory of low-frequency Alfvén modes
464 in tokamaks *Plasma Phys. Control. Fusion* **38** 2011–28
- 465 [20] Gao Z, Wang P and Sanuki H 2008 Plasma shaping effects on the geodesic acoustic
466 mode in toroidally axisymmetric plasmas *Physics of Plasmas* **15** 074502
- 467 [21] Miller R L, Chu M S, Greene J M, Lin-Liu Y R and Waltz R E 1998 Noncircular, finite
468 aspect ratio, local equilibrium model *Physics of Plasmas* **5** 973–8
- 469 [22] Chen L and Zonca F 2016 Physics of Alfvén waves and energetic particles in burning
470 plasmas *Rev. Mod. Phys.* **88** 015008
- 471 [23] Zonca F and Chen L 2014 Theory on excitations of drift Alfvén waves by energetic
472 particles. I. Variational formulation *Physics of Plasmas* **21** 072120
- 473 [24] Zonca F and Chen L 2014 Theory on excitations of drift Alfvén waves by energetic
474 particles. II. The general fishbone-like dispersion relation *Physics of Plasmas* **21** 072121
- 475 [25] Freidberg J P 2014 *Ideal MHD* (Cambridge: Cambridge University Press)
- 476 [26] Yu W, Zhou D and Xiang N 2012 A novel local equilibrium model for shaped tokamak
477 plasmas *Physics of Plasmas* **19** 072520

478 [27] Connor J W, Hastie R J and Taylor J B 1978 Shear, Periodicity, and Plasma Ballooning
479 Modes *Phys. Rev. Lett.* **40** 396–9

480 [28] Tsai S and Chen L 1993 Theory of kinetic ballooning modes excited by energetic
481 particles in tokamaks 8

482

483